Use of hydrodynamic theory to estimate electrical current redistribution in metals

E. P. Yu,[1,*] T.J. Awe,[1] K.R. Cochrane,[1] K. C. Yates,[2] T.M. Hutchinson,[3] K.J. Peterson,[1] and B. S. Bauer[3]

[1]*Sandia National Laboratories, Albuquerque, New Mexico 87185*
[2]*Los Alamos National Laboratory, Los Alamos, New Mexico 87545*
[3]*University of Nevada, Reno, Reno, Nevada 89506*

(Dated: March 20, 2020)

Using the analogy between hydrodynamic and electrical current flow, we study how electrical current density **j** redistributes and amplifies due to two commonly-encountered inhomogeneities in metals. First, we consider flow around a spherical resistive inclusion, and find significant j amplification, *independent* of inclusion size. Hence, even μm-scale inclusions can affect performance in applications by creating localized regions of enhanced Joule heating. Next, we investigate **j** redistribution due to surface roughness, idealized as a sinusoidal perturbation with amplitude A and wavelength λ. Theory predicts that j amplification is determined by the ratio A/λ, so that even "smooth" surface finishes (i.e., small A) can generate significant amplification, if λ is correspondingly small. We compare theory with magnetohydrodynamic simulation, to illustrate both the utility and limitations of the steady-state theory.

PACS numbers: Valid PACS appear here

I. INTRODUCTION

Understanding how electrical current flows through metal is essential to numerous current-driven applications, including magneto-inertial fusion [1–6], material properties studies [7–11], X-ray generation [12, 13], laboratory astrophysics [14–18], and electromagnetic power flow through magnetically-insulated transmission lines (MITLs). The problem is complicated by the inhomogeneity of metals, which include small (μm-scale), volumetrically-distributed resistive inclusions (RI) [19] and voids [20], as well as surface perturbations, such as machining grooves. While small, these imperfections will cause the current density **j** to redistribute and amplify, thus resulting in locally enhanced Joule heating.

Non-uniform heating generally degrades performance in applications. For instance, in microelectronics "current crowding" and its associated enhanced heating reduces device lifetime (e.g., Refs. [21, 22]). At larger scale, MITLs deliver multi-MA currents to a target ("load"), and are also affected by non-uniform heating. Once electrode surfaces heat to $T_d \sim 700$ K [23, 24], they thermally desorb contaminants which ionize into plasma, leading to an undesired consequence: current shunts across the anode-cathode gap before reaching the load. In simulating cm-scale MITLs, it is not feasible to resolve μm-scale surface imperfections, so modeling efforts [25–28] commonly assume a perfectly smooth metal surface. Hence, it is important to understand if enhanced heating due to RI and surface roughness allows metal to reach T_d significantly earlier than an ideal surface.

More broadly, hot spots can potentially seed the electrothermal instability [29–37], a Joule heating-driven instability which, assuming vertical current flow, manifests as horizontal, overheated striations in metals. In applications involving magnetically-accelerated conductors, striations are oriented so as to seed the virulent magneto Rayleigh-Taylor instability (e.g., Refs. [30, 38–40]), which amplifies surface deformations in-flight, reducing the integrity of the conductor.

Recent experiments [19, 41] on Joule-heated metal rods confirm the correlation between surface features and non-uniform heating, but other possible causes exist. For instance, high-energy plasma particles flow within and along the MITLs, eventually striking the load and depositing their energy, resulting in non-uniform heating [42]. In order to estimate the relative importance of different heating mechanisms, we need to develop a more quantitative understanding of how metal inhomogeneities drive j and temperature amplification. How does the amplification scale with the size of the perturbation? What numerical resolution is required to accurately simulate these perturbations?

To address these questions, we employ the analogy between steady-state electrical current flow and incompressible, potential fluid flow, which has been known for some time [43]. In this work, we illustrate the analogy by applying it to two idealized scenarios of physical relevance. First, we consider flow around a non-conducting sphere of radius R (playing the role of a void or RI), and find that maximum j amplification is 3/2, *independent* of size R. Second, we study flow over a sinusoidally-rippled surface of amplitude A and wavelength λ (an idealization of machining grooves) and find that j amplification depends on the ratio A/λ, so that even small-amplitude ripples drive significant amplification if λ is also small. The large impact of small-scale features in driving local field enhancements has also been noted in the study of radio-frequency cavities (e.g., Refs. [44, 45]).

The paper is organized as follows: in Sec. II we describe the connection between hydrodynamic and electrical current flow, focusing on the two cases of flow around

*Electronic address: epyu@sandia.gov

FIG. 1: a) Current flow around a non-conducting sphere of radius R, embedded in metal. The visualization plane cuts through the center of the sphere; the full 3D solution is obtained by rotating the 2D pattern about the z axis. Black lines represent $\mathbf{j}$ streamlines. b) $j(x)$ taken along the line $\mathcal{L}$, which lies in the equatorial plane.

an RI and flow over a rippled surface. In Sec. III, we estimate the temperature perturbation arising from local amplification in j and Joule heating. In Sec. IV we compare the analytic solutions described in Sec. II with magnetohydrodynamic (MHD) simulation. We conclude our discussion in Sec. V.

II. ANALOGY BETWEEN ELECTRICAL AND HYDRODYNAMIC FLOW

A. Current flow around a resistive inclusion (RI)

We first consider the idealized problem of steady-state electrical current flow around a sphere of radius R and zero electrical conductivity, embedded in metal (of infinite extent) with conductivity σ_0 (see Fig. 1a). Inside the metal, Ohm's law

$$\mathbf{j} = \sigma_0 \mathbf{E}, \tag{1}$$

combined with

$$\mathbf{E} = -\nabla\phi - \frac{\partial \mathbf{A}}{\partial t} \overset{\frac{\partial}{\partial t}=0}{\rightarrow} -\nabla\phi \tag{2}$$

yields

$$\mathbf{j} = -\sigma_0 \nabla\phi = -\nabla\tilde{\phi}, \tag{3}$$

where $\tilde{\phi} \equiv \sigma_0\phi$. Also, in steady state, charge conservation demands $\nabla \cdot \mathbf{j} = 0$, so $\nabla^2\tilde{\phi} = 0$. Hence, we seek a harmonic function $\tilde{\phi}$ subject to the boundary conditions $\mathbf{j} \cdot \hat{\xi}(\xi = R) = 0$, or equivalently $\frac{\partial\tilde{\phi}}{\partial\xi}(\xi = R) = 0$, and $\mathbf{j}(\xi \rightarrow \infty) = j_0\hat{z}$, which leads to $-\frac{\partial\tilde{\phi}}{\partial z}(\xi \rightarrow \infty) = j_0$.

The above problem is exactly the same as its hydrodynamic counterpart: steady-state, incompressible, ideal (i.e., viscosity $\nu \rightarrow 0$) flow around a sphere. Assuming potential flow (i.e., $\nabla \times \mathbf{v} = 0$), the flow velocity satisfies $\mathbf{v} = -\nabla\phi$, and incompressibility $\nabla \cdot \mathbf{v} = 0$ demands $\nabla^2\phi = 0$. At the boundary of the sphere $\mathbf{v} \cdot \hat{\xi}(\xi = R) = 0$ (i.e., $\frac{\partial\phi}{\partial\xi}(\xi = R) = 0$), and as $\xi \rightarrow \infty$, $\mathbf{v}$ attains its free-stream value $\mathbf{v}(\xi \rightarrow \infty) = v_0\hat{z}$ (i.e., $-\frac{\partial\phi}{\partial z}(\xi \rightarrow \infty) = v_0$).

Hence, $\mathbf{j}$ and $\mathbf{v}$ satisfy the same boundary conditions, along with Laplace's equation, thus establishing that the hydrodynamic and electrical cases are the same. To obtain the solution to the electrical problem, we simply adopt the well-known hydrodynamic solution (e.g., Ref. [46], pg 488) and substitute $\mathbf{v} \rightarrow \mathbf{j}, v_0 \rightarrow j_0$ to find

$$j_\xi = j_0 \cos\alpha (1 - \frac{R^3}{\xi^3}) \tag{4}$$

$$j_\alpha = -j_0 \sin\alpha (1 + \frac{R^3}{2\xi^3}), \tag{5}$$

valid for $\xi \geq R$.

We can quantify the current redistribution $\delta\mathbf{j}$ due to an obstacle embedded in a uniform flow $j_0\hat{z}$ by computing $\frac{\delta j}{j_0} = \frac{|\delta\mathbf{j}|}{j_0} \equiv \frac{|\mathbf{j} - j_0\hat{z}|}{j_0}$. In the case of flow around a sphere,

$$\frac{\delta j_{sphere}}{j_0} = \frac{R^3}{\xi^3}(\cos^2\alpha + \frac{\sin^2\alpha}{4})^{1/2}, \tag{6}$$

which reaches its maximum value of unity at the poles of the sphere (i.e., $\xi = R; \alpha = 0, \pi$). Here $\delta\mathbf{j}$ exactly cancels $j_0\hat{z}$, so $j(\xi = R; \alpha = 0, \pi) = 0$, in accord with the fluid interpretation of the poles as stagnation points (see Fig. 1a). Conversely, at the equator $\alpha = \frac{\pi}{2}$, $\delta\mathbf{j}$ amplifies $\mathbf{j}$, which reaches its peak value at $\xi = R$: $j(\xi = R, \alpha = \pi/2) = \frac{3}{2}j_0$. We note that Refs. [21, 33] computationally studied a very similar perturbation, and described $\delta\mathbf{j}$ qualitatively.

The solution for $\mathbf{j}$, shown in Eqs. (4-5), obeys *similarity* (e.g., pg. 57 of Ref. [47], as well as Refs. [48, 49]): spheres with different R generate the same flow pattern and amplification; R only determines how rapidly j approaches its asymptotic value j_0, via the function R^3/ξ^3. This observation has several important, albeit inconvenient, consequences: regardless of size, an RI generates significant amplification $j_{max}/j_0 = 3/2$. Furthermore, to computationally model μm-scale RI properly, we must include very fine resolution (i.e., $d\xi \ll R$) to capture the rapid R^3/ξ^3 falloff.

Focusing on the case of hydrodynamic flow $\mathbf{v}$, only in the limit of ideal flow (where the Reynolds number $Re \equiv vR/\nu \rightarrow \infty$) is the flow amplification fixed at $3/2$, independent of R. However, a real fluid possesses finite kinematic viscosity ν, representing shear stress due to intermolecular forces and collisions. In this case, the boundary condition determining the normal component of $\mathbf{v}$ at the surface of the sphere, $\mathbf{v} \cdot \hat{\xi}(\xi = R) = 0$, must be supplemented with the "no-slip" condition on the tangential component of velocity $\mathbf{v} \cdot \hat{\alpha}(\xi = R) = 0$, i.e., the fluid molecules "stick" to the stationary surface of the sphere. Now consider flow amplification in the limit of vanishing R: $R \rightarrow 0$ implies $Re \rightarrow 0$ (for finite ν), so the fluid is no longer ideal. In this limit, solution of the Navier-Stokes equation, incorporating the no-slip condition, reveals that there is no flow amplification (e.g., pg 60 of Ref. [47]).

Returning to electrical current $\mathbf{j}$, one might ask whether a similar effect occurs for sufficiently small R, due to an electrical analog of the fluid viscosity. In a conductor, electron-electron collisions indeed result in an electron viscosity ν_e. However, in a conventional

FIG. 2: a) Cross-sectional view of fully-diffused flow of $\mathbf{j}$ over sinusoidally-perturbed rod, with outer boundary defined by $r = r_0 - A\sin(2\pi z/\lambda)$. b) In a perfectly-conducting, sinusoidally-perturbed rod, surface current K is restricted to a skin depth $\delta \ll A, \lambda$.

metal, $\nu_e \to 0$ because the electron-electron collision rate is dwarfed by electron collisions with the stationary ionic lattice. The scattering of electrons due to the lattice, driven primarily by lattice vibrations (phonons) and impurities, constitute the metal's electrical resistivity $\eta \equiv 1/\sigma$, which is accounted for in Ohm's law, Eq. (1). In this case of a resistive metal, to the best of our knowledge there is no equivalent of the no-slip condition on electrons flowing past a non-conducting boundary. Consequently, we only specify the normal component of $\mathbf{j}$ on the RI's surface (i.e., $\mathbf{j}\cdot\hat{\xi}(\xi = R) = 0$), and current flow in a resistive metal is equivalent to *ideal* fluid flow, as shown at the beginning of this section. Consequently, so long as we avoid quantum effects by restricting $R \gg \lambda_d$ (the electron de Broglie wavelength ≤ 1 nm for aluminum), we expect maximum flow amplification to satisfy $j_{max}/j_0 = 3/2$.

In ultraclean materials (e.g., graphene), conditions can be achieved where the situation described above reverses: electron-lattice scattering occurs so infrequently that electron-electron interactions dominate, giving rise to non-negligible electron viscosity ν_e. In this regime, electrons indeed behave as a viscous fluid, and Eq. (1) must be replaced by a Navier-Stokes-like equation [50]. Experiments have demonstrated signatures of viscous electron flow, e.g., parabolic-shaped Poiseuille flow (characteristic of viscous flow through pipes) [51] and vortex formation [52]. Furthermore, simulations predict that flow around an obstacle generates vortex shedding [53], just as in a fluid. However, in this work we focus on conventional metals, where Ohm's law and the ideal fluid analogy apply.

Before closing this section, we note that when we allow finite electrical conductivity σ in the RI, the problem is still analytically tractable. The boundary condition $\mathbf{j}\cdot\hat{\xi}(\xi = R) = 0$ is replaced by continuity of j_ξ and ϕ across the RI surface: $\mathbf{j}\cdot\hat{\xi}(\xi = R^-) = \mathbf{j}\cdot\hat{\xi}(\xi = R^+)$ and $\phi(\xi = R^-) = \phi(\xi = R^+)$. In this case, the fluid analogy of flow around an impenetrable sphere fails, but is replaced by the analogy with fields in a linear dielectric, as demonstrated in §7.5 of Ref. [54].

B. Current flow over rippled surface

The hydrodynamic analogy applies not only to resistive objects embedded in the metal, but also deformations of the metal surface. The surface finish of metal rods commonly exhibit periodic grooves as a result of the fabrication process (e.g., Ref. [55]), which may be idealized with a sinusoidally-perturbed surface $r_s = r_0 - A\sin(\frac{2\pi z}{\lambda})$, as illustrated in Fig. 2a. Assuming fully-diffused, steady-state $\mathbf{j}$, within the metal $\nabla\cdot\mathbf{j} = 0 \Rightarrow \nabla^2\tilde{\phi} = 0$, just as in the discussion in Sec. II A. At the metal/vacuum boundary, $\mathbf{j}\cdot\mathbf{n} = 0$, where $\mathbf{n}$ is the normal vector at the boundary (see Fig. 2a). As we shall see below, the characteristic radial scale length of the solution is λ, so the unperturbed current density j_0 is reached as $\frac{r_0-r}{\lambda}$ increases: $\mathbf{j}(\frac{r_0-r}{\lambda} \to \infty) = j_0\hat{\mathbf{z}}$.

In the limit $\lambda \ll r_0$, the problem is quasi-planar, i.e., spatial variations in $\mathbf{j}$ are confined to a radial region $\Delta r \sim \lambda$, and if $r_0/\Delta r \gg 1$, we can ignore the rod curvature. In this case, we can use the planar hydrodynamic solution for steady-state, incompressible, potential flow over an impermeable sinusoidal wall. As before, the hydrodynamic velocity $\mathbf{v} = -\nabla\phi$ satisfies the same equation (i.e., $\nabla^2\phi = 0$) and boundary conditions as the electrical problem. A perturbation solution exists (e.g., Ref. [56], pg. 353), correct to first order in perturbation parameter $\frac{A}{\lambda} \ll 1$, so we consider small "waviness". As in Sec. II A, this directly yields the corresponding electrical flow solution:

$$j_r/j_0 = -kA\cos(kz)\mathrm{e}^{-k(r_0-r)}, \tag{7}$$

where $k = 2\pi/\lambda$, and

$$j_z/j_0 = 1 + kA\sin(kz)\mathrm{e}^{-k(r_0-r)} \equiv 1 + \frac{\delta j_z}{j_0}. \tag{8}$$

Note $j = \sqrt{j_r^2 + j_z^2}$ satisfies

$$j/j_0 \simeq 1 + kA\sin(kz)\mathrm{e}^{-k(r_0-r)} = 1 + \frac{\delta j_z}{j_0}, \tag{9}$$

reaching a maximum at the valleys of the rod surface

$$j_{max}/j_0 \simeq 1 + kA = 1 + \frac{2\pi A}{\lambda}, \tag{10}$$

and a minimum in the bulges

$$j_{min}/j_0 \simeq 1 - kA = 1 - \frac{2\pi A}{\lambda}, \tag{11}$$

as illustrated in Fig. 2a. The current perturbation exponentially decays as we move away from the rod surface, with characteristic length scale $\lambda/2\pi$, similar to the solution for deep water gravity waves (e.g., §18.18 of Ref. [56]). The j amplification expressed in Eq. (10) may help explain earlier-than-expected plasma formation in experiments on current-driven rods in Ref. [57].

We can also consider current amplification in the limit of a *perfectly conducting* rod, again with radius $r_s = r_0 - A\sin(\frac{2\pi z}{\lambda})$, but now the current skin depth $\delta \ll A, \lambda$ (see Fig. 2b). The perfect conductor assumption is commonly used in magneto Rayleigh-Taylor (e.g., Ref. [38]) and MHD (e.g., Ref. [58]) instability analysis. As before, we consider the small amplitude limit $\frac{A}{\lambda} \ll 1, \frac{A}{r_0} \ll 1$.

Applying Ampère's law at the rod surface, we find $\mathbf{B}(r = r_s) = B_\theta(r_s)\hat{\theta}$, where

$$B_\theta(r_s) = \frac{\mu_0 I}{2\pi(r_0 - A\sin(kz))} \simeq B_0(1+\frac{A}{r_0}\sin(kz)), \quad (12)$$

and $B_0 = \frac{\mu_0 I}{2\pi r_0}$. This expression, valid in both the perfectly-conducting (Fig. 2b) and fully-diffused (Fig. 2a) limits, shows that small amplitude ripples generate a correspondingly small perturbation in B.

In a perfect conductor, we can compute the surface current $\mathbf{K}$ through the boundary condition

$$\mu_0\mathbf{K} = \mathbf{n} \times \mathbf{B}(r_s), \quad (13)$$

where the normal vector $\mathbf{n}$ satisfies

$$\mathbf{n} = \hat{r} + kA\cos(kz)\hat{z}. \quad (14)$$

Combining Eqs. (12-14) we obtain the surface current, valid to first order,

$$\frac{\mathbf{K}}{K_0} \simeq -\hat{r}kA\cos(kz) + \hat{z}(1+\frac{A}{r_0}\sin(kz)), \quad (15)$$

where $K_0 = B_0/\mu_0$ is the unperturbed surface current. The maximum surface current is reached in the valley

$$\frac{K_{max}}{K_0} \simeq 1 + \frac{A}{r_0}, \quad (16)$$

so that for typical values of A and r_0 satisfying $A/r_0 \ll 1$, K amplification is negligible in a perfect conductor, as is the perturbation in B (see Eq. (12)).

In contrast, the solution for fully-diffused j in Eqs. (7-8) resolves the bunching and expansion of $\mathbf{j}$ streamlines as they travel over the rippled surface, as illustrated in Fig. 2a. Consequently, j amplification depends on $\frac{A}{\lambda}$ (rather than $\frac{A}{r_0}$), so even "small" A satisfying $A/r_0 \ll 1$ can generate significant j amplification (if λ is correspondingly small), unlike the perfectly conducting limit.

We now estimate current amplification due to surface roughness and RI. Consider the beryllium liners studied in Ref. [55], machined to obtain a high-quality surface finish: root-mean-square roughness $A \sim 0.175\mu$m, $\lambda \sim 3$ μm. The skin depth will rapidly exceed A and λ, invalidating the perfect conductor assumption. In this case, Eqs. (7-8) are more applicable, so $\frac{j_{max}}{j_0} \sim 1+\frac{2\pi A}{\lambda} \sim 1.37$, i.e., non-negligible and fairly close to the peak $\frac{j_{max}}{j_0} \sim 1.5$ due to the RI. However, for similarly-machined (smooth) aluminum rods studied in Ref. [59], $A \sim 0.01\mu$m, $\lambda \sim 1.25$ μm, $\frac{j_{max}}{j_0} \sim 1.05$, significantly smaller than that due to RI.

C. Applicability of hydrodynamic analogy

The connection between electrical and hydrodynamic flow was established under the assumption of steady-state conditions. However, when current $I(t)$ is applied to a metal, magnetic field $\mathbf{B}$ and $\mathbf{j}$ gradually diffuse through the surface, thus introducing both temporal and spatial dependence into $\mathbf{j}(r,t)$ (r is the radial coordinate, as in Fig. 2). More specifically, Eq. (3) now generalizes to

$$\mathbf{j} = -\sigma_0\left(\nabla\phi + \frac{\partial\mathbf{A}}{\partial t}\right). \quad (17)$$

The inductive component of electric field $\frac{\partial\mathbf{A}}{\partial t}$ generates eddy currents resisting the penetration of field into metal, as well as introduces "vorticity"

$$\nabla \times \mathbf{j} = -\sigma_0\frac{\partial\mathbf{B}}{\partial t}. \quad (18)$$

We can understand the physical meaning of Eq. (18) by using Ampère's law $\nabla \times \mathbf{B} = \mu_0\mathbf{j}$ to obtain the familiar magnetic diffusion equation

$$\frac{\partial\mathbf{B}}{\partial t} = \frac{1}{\mu_0\sigma_0}\nabla^2\mathbf{B}. \quad (19)$$

The solution of Eq. (19) (e.g., Ref. [60]) shows that as $\mathbf{j}(r,t)$ diffuses into the metal, the spatial scale on which it varies is the skin depth δ, which generally increases with time (e.g., $\delta \sim 2\sqrt{t/\mu_0\sigma_0}$ for I = const). Focusing on the RI case, the complication of a spatially and temporally-varying $\mathbf{j}$ contradicts the assumption of a sphere immersed in a spatially-*uniform*, time-*independent* flow. However, in the limit $\delta \gg R$, $\mathbf{j}$ varies slowly enough relative to the RI spatial scale that we can view the RI as immersed in an approximately uniform flow, thus recovering the analogy between hydrodynamic and electrical flow.

In the time-varying case, we must also consider the time-dependent form of charge conservation: $\nabla \cdot \mathbf{j} = -\frac{\partial\rho_q}{\partial t}$, where ρ_q is the electric charge density. Combining this with Ohm's law (1) and Gauss's law $\nabla \cdot \mathbf{E} = \frac{\rho_q}{\epsilon_0}$, we obtain

$$\frac{\sigma_0}{\epsilon_0}\rho_q = -\frac{\partial\rho_q}{\partial t}, \quad (20)$$

with solution $\rho_q = \rho_q(0)\mathrm{e}^{-\frac{\sigma_0}{\epsilon_0}t}$, i.e., charge in the conductor will dissipate, by running to the metal boundary, on very fast time scale $\frac{\epsilon_0}{\sigma_0}$ ~1e-18 s, for $\sigma_0 \sim 1e7(\Omega m)^{-1}$. This time scale is sufficiently fast that for most applications, we can assume $\rho_q \sim 0$ and $\nabla \cdot \mathbf{j} = 0$, so the steady state condition is recovered. In obtaining Eq. (20), which is commonly derived in textbooks (e.g., Ref. [61]), we have assumed $\sigma = \sigma_0$ is constant. This approximation only holds when Joule heating is sufficiently low so as to not alter σ through $\sigma(T)$ dependence, and will be relaxed in the following section.

III. TEMPERATURE PERTURBATION

To understand the effect of the current perturbation $\delta\mathbf{j} \equiv \mathbf{j} - \mathbf{j_0}$ on the corresponding temperature perturba-

tion, we first note

$$j^2 = j_0^2 + 2\mathbf{j_0}\cdot\delta\mathbf{j} + \delta j^2 = j_0^2 + 2j_0\delta j_z + \delta j^2, \quad (21)$$

where in the last equality we assume $\mathbf{j_0} = j_0\hat{z}$. Plugging this into the the energy equation, we obtain

$$\rho c_V \frac{\partial T}{\partial t} = \eta(T) j^2 = \eta(T) j_0^2 \left(1 + 2\frac{\delta j_z}{j_0} + \frac{\delta j^2}{j_0^2}\right), \quad (22)$$

where $\rho, c_V, T, \eta \equiv 1/\sigma$ correspond to the density, specific heat, temperature, and resistivity, respectively. In Eq. (22) we have ignored thermal conduction for simplicity. In order to integrate Eq. (22), we employ the convenient and commonly-used approximation for the pre-melt temperature dependence of resistivity $\eta(T) \simeq \frac{d\eta}{dT}T$, where $\frac{d\eta}{dT}$ is a constant [31, 60, 62]. Then assuming $\rho, c_V, j_0, \delta j$ all constants in time (for illustrative purposes), Eq. (22) predicts exponential growth:

$$T(x,t) = T_i \mathrm{e}^{\gamma t\left(1+2\frac{\delta j_z}{j_0}+\frac{\delta j^2}{j_0^2}\right)}, \quad (23)$$

where $T_i = T(t=0)$ and $\gamma = \frac{\frac{d\eta}{dT} j_0^2}{\rho c_V}$ is the electrothermal instability growth rate for striations [30, 31]. Furthermore, locations with $\delta j_z(x) > 0$ will grow at an effectively faster growth rate $\gamma(1 + 2\frac{\delta j_z(x)}{j_0} + \frac{\delta j(x)^2}{j_0^2})$.

To illustrate the importance of current redistribution $\delta\mathbf{j}$, we first consider the case where $\delta\mathbf{j} = 0$, but we allow an initial temperature perturbation $\delta T_i > 0$. The temperature in the initially hotter region will follow $T_h = (T_i + \delta T_i)\mathrm{e}^{\gamma t}$, whereas the temperature in the ambient metal obeys $T_0 = T_i\mathrm{e}^{\gamma t}$. Hence, the temperature difference $\Delta T \equiv T_h - T_0 = \delta T_i \mathrm{e}^{\gamma t}$ grows exponentially. However, the *relative* temperature difference $\Delta T/T_0 = \delta T_i/T_i$ is fixed at the initial value and shows no growth, as discussed in Ref. [37].

In contrast, current redistribution *does* allow a growing $\Delta T/T_0$. To show this, we assume no initial temperature perturbation ($\delta T_i = 0$), but we allow $\delta j_z > 0$. The temperature in the region with amplified j obeys $T_h = T_i \mathrm{e}^{\gamma t(1+2\frac{\delta j_z}{j_0}+\frac{\delta j^2}{j_0^2})}$, while the temperature in the ambient metal again follows $T_0 = T_i\mathrm{e}^{\gamma t}$. Hence, in the limit $\frac{\delta j}{j_0} \ll 1$,

$$\Delta T/T_0 \simeq \mathrm{e}^{2\gamma t\frac{\delta j_z}{j_0}} - 1, \quad (24)$$

i.e., the relative temperature difference grows at the effective growth rate $\gamma_{eff} = 2\gamma\frac{\delta j_z}{j_0}$.

The foregoing discussion ignores an important physical effect: the enhanced Joule heating associated with a region with $\delta j_z > 0$ results in larger T, as well as η (owing to the $\eta(T)$ dependence), which in turn causes further j redistribution *out* of this region. Due to this feedback loop, which has been studied in 1D in the nonlinear magnetic diffusion problem [60, 62, 63], the assumption of $j(x)$ fixed in time is an oversimplification to the true scenario where $j(x)$ and $\eta(x)$ are ever-changing. We have studied this 3D process in detail, and will report on it in the follow-on publication.

FIG. 3: a) Current $I(t)$ used to drive MHD simulation. b) Doubly-periodic wedge used to model $r_0 = 500$ μm Al rod, with hemispherical resistive inclusion (RI) embedded on outer face. Also shown are visualization planes FRONT, viewing the outer surface of the rod from along the radial $\hat{r}$ direction, and TOP, viewing the axial midplane $z_m = 35\mu$m (bounded by the blue dotted lines).

FIG. 4: a) Front view of 3D MHD simulation with $R = 3\mu$m inclusion, at outer radius $r = 500\mu$m and t=75 ns. This simulation is run without hydrodynamics and is driven by constant I=6 kA current. b) Top view, showing equatorial plane. c) Comparison of j along the line $\mathcal{L}$ in a), for $R = 3\mu$m and $R = 6\mu$m inclusions, with theoretical predictions. Blue dots are from a lower resolution simulation.

IV. COMPARISON WITH MHD SIMULATION

A. Hemispherical resistive inclusion (RI)

This work was motivated by experiments described in Ref. [19], in which a current pulse (see Fig. 3a) was applied to aluminum rods of radius r_0 =500 μm. Hence, MHD simulations of this scenario, run using the code Alegra [64], will serve as our testbed for comparison to theory. We use a SESAME equation of state [65], including material strength (elastic-plastic constitutive model combined with Steinberg-Guinan-Lund yield model), to simulate the Al rod, which is initialized at room temperature T=294 K (all units are SI). Electrical and thermal conductivities are provided by the Lee-More-Desjarlais model [66]. Simulations assume ion and electron temperatures are equal ($T_i = T_e \equiv T$) and do not account for radiative transport or losses. To keep the (Eulerian) computational domain tractable, we only model a small section of the rod, using the 3D wedge geometry shown in Fig. 3b. We assume periodic boundary conditions in both the axial (z) and azimuthal (θ) directions. As shown in Fig. 3b, on the outer face of the rod, we embed a hemispherical RI of radius $R = 3\mu$m. For simplicity, we model the RI as Al, with electrical and thermal conductivity reduced by 1e6, to simulate the non-conducting

FIG. 5: a) Front view of 3D MHD simulation with $R = 3\mu$m inclusion, at outer radius $r = 500.25$ μm and t=30 ns. This simulation is driven by $I(t)$ and allows hydrodynamic expansion. b) Top view. c) Comparison of j(t=30 ns) along the line $\mathcal{L}$ with theoretical prediction. d) Same, but taken along the radial lineout $\mathcal{L}'$. e) Same as c), but showing the results of 3 different values of R. f) same as d), but showing 3 different values of R, in addition to an unperturbed simulation (i.e., RI is absent).

FIG. 6: a) Cross-sectional view of 2D simulation of sinusoidally-perturbed rod, run without hydrodynamics and driven by I=6 kA, at t =75 ns. b) Comparison of simulation and theory along radial lineouts through the hill and valley for $\lambda = 6\mu$m, A=0.25 μm. c) Same for $\lambda = 12\mu$m, A=0.5 μm, demonstrating similarity. d) Same for $\lambda = 6\mu$m, $A = 0.5\mu$m, illustrating discrepancy between theory and simulation. e) Same for $\lambda = 6\mu$m, $A = 1\mu$m.

FIG. 7: a) $j(t = 30$ ns) from simulation driven by $I = I(t)$ and run with hydrodynamics, for $\lambda = 6\mu$m, $A = 0.5\mu$m. Magenta curve shows $j_0(r)$ from a rod with no sinusoidal perturbation. b) Same as a), but adding results from 2 other simulations, to test similarity.

material assumed in the theory. Note that the solution for flow around a sphere is still applicable to our hemispherical scenario, since the 3D solution described in Sec. II A is symmetric about a plane cutting through the center of the sphere.

As described in Sec. II C, the steady-state assumption of hydrodynamic theory is inconsistent with the time-varying magnetic diffusion solution. However, if the current skin depth $\delta \gg R$, then the hydrodynamic theory is approximately valid. To provide the most favorable conditions for comparison between theory and simulation, we first consider constant $I = I_0$ =6 kA (rather than $I(t)$ in Fig. 3a) and wait sufficiently long time τ so that $\delta \gg R$. We choose sufficiently low value of I_0 so that on the time scale τ, Joule heating remains negligible, thus avoiding the feedback loop described in Sec. III. Low I_0 results in negligible expansion (through Joule heating) and compression (through $\mathbf{j} \times \mathbf{B}$ force). Nevertheless, we suppress hydrodynamics in these simulations, again in the interest of best matching the assumptions of theory.

Simulation results in Figs. 4a,b illustrate j amplification around the equator of the RI, in qualitative agreement with the theoretical solution in Fig. 1. Furthermore, as seen in the top view in Fig. 4b, by $t = 75$ ns the radial variation in j due to magnetic diffusion is weak: other than the red annulus due to the RI, j is approximately uniform. Hence, enough time has passed that $\delta \gg R$, validating the approximation of an RI embedded in a uniform flow $\mathbf{j} = j_0\hat{z}$.

In Fig. 4c, we quantitatively compare j from simulation (black line, labelled $R = 3\mu$m), taken along the azimuthal lineout $\mathcal{L}$ shown in Fig. 4a, with the theoretical prediction (dashed green line). For this simulation, which uses fine resolution ($\delta x \sim 0.1\mu$m) in the vicinity of the RI, we find close agreement. However, a lower resolution case using $\delta x \sim 0.5\mu$m (see blue dots in Fig. 4c) does not possess sufficient resolution to capture the peak of the rapidly-varying solution $j = j_0(1 + \frac{R^3}{2x^3})$. This illustrates the challenge of computationally modelling μm-scale RI: we must use resolution $\delta x \ll R$ to capture the solution.

On the other hand, as mentioned in Sec. II A, similarity suggests we can explore current redistribution around μm-scale RI, which are difficult to experimentally diagnose owing to their small size, by studying a larger, more easily-diagnosable RI. This principle is illustrated in Fig. 4c: simulation of a $R = 6\mu$m RI (solid black line) generates the same j amplification as the $R = 3\mu$m RI, in agreement with theory (red line); larger R only increases decay length.

Thus far, we have restricted simulation conditions to best match the assumptions of theory. In the simulations shown in Fig. 5, we relax these constraints, allowing time-dependent $I(t)$ (see Fig. 3a) and full MHD physics, including hydrodynamic expansion. However, we compare simulation and theory at early time t =30 ns, before Joule heating results in significant heating and modification of the $\sigma(r)$ profile. As seen in Fig. 5a,c the simulation and theory still match closely on the outer face of the rod. However, in Fig. 5b, the time-varying $I(t)$ results in skin depth $\delta \sim R$, as reflected in the noticeable radial variation in $j(r)$, in contrast to the constant I case in Fig. 4b. Hence, the assumption of a sphere placed in a uniform flow $\mathbf{j} = j_0\hat{z}$ is broken, resulting in the discrepancy in theory and simulation in Fig. 5d.

Continuing our investigation of simulations including time-varying $I(t)$, resistive diffusion, and hydrodynamic expansion, we now address the validity of similarity, which was derived under the assumption of steady-state conditions. In Fig. 5e, we reproduce the azimuthal lineout from Fig. 5c, but also include results from two simulations with larger RI. The profiles again show similarity: j_{max} (i.e., maximum j amplification) is independent of R, which only determines the decay scale length. In Fig. 5f, we reproduce the radial lineout $j(r)$ from Fig. 5d, but now include the $R = 6, 12\mu$m results, as well as $j_0(r)$, representing $j(r)$ in the absence of the RI (magenta curve). Now j_{max} *does* depend on R, thus breaking similarity. Also, somewhat non-intuitively, *smaller* R generates *larger* j_{max} at the back of the RI. Figure 5f suggests that j amplification occurs relative to the unperturbed value $j_0(r)$ at the back of the RI. Hence, the largest RI (i.e., $R = 12\mu$m) penetrates deepest into the metal, thus sampling the lowest value of $j_0(r)$ and producing the lowest j_{max}. Conversely, the smallest RI (i.e., $R = 3\mu$m) samples the largest value of $j_0(r)$, close to the surface of the rod, and generates the largest j_{max}.

B. Sinusoidally-perturbed surface

In Fig. 6a we show a 2D (r, z) simulation of an Al rod with a sinusoidal perturbation of amplitude A and wavelength λ applied to the outer surface: $r = r_0 + A\sin(\frac{2\pi}{\lambda}z)$, with $r_0 = 500$ μm. For computational savings, we only model a single wavelength λ, and apply periodic boundary conditions in the axial direction. As in the previous discussion in Sec. IV A, we initially consider simulations

with constant I =6 kA and no hydrodynamics, to most closely satisfy the assumptions of the theory in Sec. II B. In Fig. 6b, we consider the case $\lambda = 6\mu$m, $A = 0.25\mu$m (comparable to experimental values in Ref. [55]), and sample the simulation along two radial lineouts, located in the valley and hill of the perturbed surface (see Fig. 6a). Both lineouts show close agreement with theory (see Eq. (9)). In Fig. 6c, we show the same comparison for the case where both λ and A are doubled: $\lambda = 12\mu$m, $A = 0.5\mu$m. In accord with theory, this simulation exhibits longer decay length than Fig. 6b, but the same j amplification, thus verifying the similarity principle.

Unlike the exact solution in Sec. II A, the solution for flow over a rippled surface is only valid for $\epsilon \equiv A/\lambda \ll 1$. This condition is well-satisfied for the case in Fig. 6b ($\epsilon = 1/24$), resulting in close agreement between simulation and theory. In Fig. 6d we show results of an identical simulation, except A is doubled, resulting in discrepancy between theory and simulation. In Fig. 6d, we further increase A so that $kA \sim 1$, at which point we are clearly outside the bounds of linear theory, since the j perturbation in Eqs. (10-11) is equal to the unperturbed value.

Theory is also limited by the steady-state assumption. Figure 7a shows results of a simulation in which we relax this constraint, running with $I(t)$ shown in Fig. 3a, and allowing for hydrodynamic expansion. As was discussed in Sec. IV A, the skin depth δ associated with the time-varying $I(t)$ does not satisfy $\delta \gg \lambda$, resulting in a spatially-varying background flow $j_0(r)$ (see magenta curve in Fig. 7a), obtained from a 1D (i.e., unperturbed) simulation. This discrepancy with the theoretical assumption j_0=const results in the differences between theory and simulation shown in Fig. 7a.

Nevertheless, theory is still useful in estimating the maximum j amplification through Eq. (10): $j_{max}/j_0 \simeq 1+2\pi A/\lambda = 1+2\pi(0.5/6) \sim 1.5$. Here, j_0 is the constant, unperturbed value of j assumed in the theory, which isn't well-defined in the time-dependent $I(t)$ case, due to spatial variation in $j_0(r)$. However, if we approximate j_0 with its value at the rod surface ∼1.4e11 (see magenta curve in Fig. 7a), then the maximum j amplification in simulation is $j_{max}/j_0 \sim 2/1.4 \sim 1.4$, in close agreement with theory (i.e., 1.5) and confirming that small-amplitude ripples can drive significant j_{max}/j_0. We contrast this estimate with that from perfectly conducting theory: $K_{max}/K_0 \sim 1 + A/r_0 \sim 1 + 0.5/500 = 1.001$.

Continuing our study of simulations driven with time-dependent $I(t)$ and allowing hydrodynamic expansion, we consider the robustness of similarity. Figure 7b shows j(t=30 ns) from three simulations varying (A, λ) but keeping the similarity parameter $\epsilon \equiv A/\lambda$ fixed; thus, in the steady-state limit $\lambda \ll \delta$, we expect j_{max} to remain invariant. Figure 7b illustrates that even in the time-varying case, simulations demonstrate approximate similarity: j_{max} varies weakly ($\sim 10\%$) despite (A, λ) varying by a factor of 16. As in the case of the RI, smaller (A, λ) results in larger j_{max}, and we offer the same explanation: smaller A samples larger values of $j_0(r)$, closer to the rod surface, thus producing larger j_{max}.

In Ref. [59], researchers applied 20 MA to Al rods with pre-machined sinusoidal perturbations, in which (A, λ) were varied, while keeping ϵ fixed. Later-time radiography between the $\lambda = 200\mu m, A = 5\mu m$ and $\lambda = 400\mu m, A = 10\mu m$ cases did not show similarity, with the smaller λ exhibiting enhanced heating and expansion, in qualitative agreement with Fig. 7b. We anticipate that smaller values of λ will better satisfy a key requirement for similarity (i.e. $\lambda \ll \delta$), and indeed $\lambda = 25, 50, 100\mu$m *do* show evidence for similarity in Fig. 8a of Ref. [59]. Further investigation is required.

V. CONCLUSION

We have used hydrodynamic solutions to understand electrical current flow around obstacles and surface features. We focused on two simple, idealized scenarios (i.e., spherical RI and sinusoidal surface roughness), but the vast collection of hydrodynamic solutions allows consideration of more complicated perturbations, such as ellipsoidal RI. While the theory is derived under very stringent assumptions (e.g., steady-state, spatially-constant background flow j_0) that are not generally satisfied in the electrical problem, in Sec. IV we show approximate agreement with MHD simulation even in the time-varying case. In particular, simulations confirm a main finding of the theory: even physically small perturbations can drive significant j amplification.

In the simulations in Sec. IV, we have avoided the case where j is sufficiently intense so as to drive appreciable increase in temperature δT. As described in Sec. III, due to the temperature dependence of electrical conductivity $\sigma(T)$, a local increase δT results in $\delta\sigma < 0$, which causes **j** and Joule heating to redistribute, driving a newly-overheated region and further **j** redistribution. Consequently, the "topography" σ and flow **j** are constantly evolving, allowing our original perturbation (e.g., spherical RI) to grow in size and transform structurally with time. This dynamical process will be covered in a future paper; we will find that even in this complex scenario, the hydrodynamic analogy still proves useful.

Acknowledgments

We benefitted from stimulating discussion with D. Ryutov, M. Desjarlais, Y.Y. Lau, A.Velikovich, D. Sinars, L. Ellison, J. Chittenden, D. Ruiz, M. Weis, R. Vesey, M. Hatch, T. Mattsson, and T. Eisenberg. We thank T. Sjostrom and S. Crockett for graciously providing their EOS table, and E. Harding and K. Tomlinson for sharing their research on voids in beryllium. EPY thanks E. Waisman, B. Hutsel, N. Bennett, and M. Cuneo for discussions on MITL physics; A. C. Robinson for Alegra guidance; and the anonymous referees for improving the manuscript, through their suggestions

and questions. Sandia National Laboratories is a multimission laboratory managed and operated by National Technology and Engineering Solutions of Sandia LLC, a wholly owned subsidiary of Honeywell International Inc. for the U.S. Department of Energy's National Nuclear Security Administration under contract DE-NA0003525.

[1] S. A. Slutz, M. C. Herrmann, R. A. Vesey, A. B. Sefkow, D. B. Sinars, D. C. Rovang, K. J. Peterson, and M. E. Cuneo, Phys. Plasmas **17**, 056303 (2010).
[2] M. R. Gomez, S. A. Slutz, A. B. Sefkow, D. B. Sinars, K. D. Hahn, S. B. Hansen, E. C. Harding, P. F. Knapp, P. F. Schmit, C. A. Jennings, T. J. Awe, M. Geissel, D. C. Rovang, G. A. Chandler, G. W. Cooper, M. E. Cuneo, A. J. Harvey-Thompson, M. C. Herrmann, M. H. Hess, O. Johns, D. C. Lamppa, M. R. Martin, R. D. McBride, K. J. Peterson, J. L. Porter, G. K. Robertson, G. A. Rochau, C. L. Ruiz, M. E. Savage, I. C. Smith, W. A. Stygar, and R. A. Vesey, Phys. Rev. Lett. **113**, 155003 (2014).
[3] M. E. Cuneo, M. C. Herrmann, D. B. Sinars, S. A. Slutz, W. A. Stygar, R. A. Vesey, A. B. Sefkow, G. A. Rochau, G. A. Chandler, J. E. Bailey, J. L. Porter, R. D. McBride, D. C. Rovang, M. G. Mazarakis, E. P. Yu, D. C. Lamppa, K. J. Peterson, C. Nakhleh, S. B. Hansen, A. J. Lopez, M. E. Savage, C. A. Jennings, M. R. Martin, R. W. Lemke, B. W. Atherton, I. C. Smith, P. K. Rambo, M. Jones, M. R. Lopez, P. J. Christensen, M. A. Sweeney, B. Jones, L. A. McPherson, E. Harding, M. R. Gomez, P. F. Knapp, T. J. Awe, R. J. Leeper, C. L. Ruiz, G. W. Cooper, K. D. Hahn, J. McKenney, A. C. Owen, G. R. McKee, G. T. Leifeste, D. J. Ampleford, E. M. Waisman, A. Harvey-Thompson, R. J. Kaye, M. H. Hess, S. E. Rosenthal, and M. K. Matzen, IEEE Trans. Plasma Sci. **40**, 3222 (2012).
[4] A. B. Sefkow, S. A. Slutz, J. M. Koning, M. M. Marinak, K. J. Peterson, D. B. Sinars, and R. A. Vesey, Phys. Plasmas **21**, 072711 (2014).
[5] I. R. Lindemuth, Phys. Plasmas **22**, 122712 (2015).
[6] V. Mokhov, O. Burenkov, A. Buyko, S. Garanin, S. Kuznetsov, V. Mamyshev, A. Startsev, and V. Yakubov, Fusion Eng. Des. **70**, 35 (2004).
[7] R. W. Lemke, M. D. Knudson, K. R. Cochrane, M. P. Desjarlais, and J. R. Asay, J. Phys.: Conf. Ser. **500**, 152009 (2014).
[8] M. R. Martin, R. W. Lemke, R. D. McBride, J. P. Davis, D. H. Dolan, M. D. Knudson, K. R. Cochrane, D. B. Sinars, I. C. Smith, M. Savage, W. A. Stygar, K. Killebrew, D. G. Flicker, and M. C. Herrmann, Phys. Plasmas **19**, 056310 (2012).
[9] P. A. Gourdain, M. B. Adams, M. Evans, H. R. Hasson, R. V. Shapovalov, J. R. Young, and I. West-Abdallah, Phys. Plasmas **26**, 042706 (2019).
[10] S. N. Bland, Ya. E. Krasik, D. Yanuka, R. Gardner, J. MacDonald, A. Virozub, S. Efimov, S. Gleizer, and N. Chaturvedi, Phys. Plasmas **24**, 082702 (2017).
[11] M. D. Knudson, M. P. Desjarlais, A. Becker, R. W. Lemke, K. R. Cochrane, M. E. Savage, D. E. Bliss, T. R. Mattsson, and R. Redmer, Science **348**, 1455 (2015).
[12] B. Jones, C. A. Coverdale, C. Deeney, D. B. Sinars, E. M. Waisman, M. E. Cuneo, D. J. Ampleford, P. D. Lepell, K. R. Cochrane, J. W. Thornhill, J. P. Apruzese, A. Dasgupta, K. G. Whitney, R. W. Clark, and J. P. Chittenden, Phys. Plasmas **15**, 122703 (2008).
[13] D. J. Ampleford, C. A. Jennings, B. Jones, S. B. Hansen, M. E. Cuneo, C. A. Coverdale, M. C. Jones, T. M. Flanagan, M. Savage, W. A. Stygar, M. R. Lopez, J. P. Apruzese, J. W. Thornhill, J. L. Giuliani, and Y. Maron, Phys. Plasmas **20**, 103116 (2013).
[14] S. V. Lebedev, A. Frank, and D. D. Ryutov, Rev. Modern Physics **91**, 025002 (2019).
[15] J. E. Bailey, T. Nagayama, G. P. Loisel, G. A. Rochau, C. Blancard, J. Colgan, Ph. Cosse, G. Faussurier, C. J. Fontes, F. Gilleron, I. Golovkin, S. B. Hansen, C. A. Iglesias, D. P. Kilcrease, J. J. MacFarlane, R. C. Mancini, S. N. Nahar, C. Orban, J. -C. Pain, A. K. Pradhan, M. Sherrill, and B. G. Wilson, Nature **517**, 56 (2015).
[16] T. Nagayama, J. E. Bailey, G. P. Loisel, G. S. Dunham, G. A. Rochau, C. Blancard, J. Colgan, Ph. Cosse, G. Faussurier, C. J. Fontes, F. Gilleron, S. B. Hansen, C. A. Iglesias, I. Golovkin, D. P. Kilcrease, J. J. MacFarlane, R. C. Mancini, R. M. More, C. Orban, J. -C. Pain, M. E. Sherrill, and B. G. Wilson, Phys. Rev. Lett. **122**, 235001 (2019).
[17] G. P. Loisel, J. E. Bailey, D. A. Liedahl, C. J. Fontes, T. R. Kallman, T. Nagayama, S. B. Hansen, G. A. Rochau, R. C. Mancini, and R. W. Lee, Phys. Rev. Lett. **119**, 075001 (2017).
[18] M. -A. Schaeuble, T. Nagayama, J. E. Bailey, T. A. Gomez, M. H. Montgomery, and D. E. Winget, Astrophys. J. **885**, 86 (2019).
[19] T. J. Awe, E. P. Yu, K. C. Yates, W. G. Yelton, B. S. Bauer, T. M. Hutchinson, S. Fuelling, and B. B. McKenzie, IEEE Trans. Plasma Sci. **45**, 584 (2017).
[20] T. Sakurai, Y. Kohmura, A. Takeuchi, Y. Suzuki, S. Goto, and T. Ishikawa, AIP Conference Proceedings **879**, 1380 (2007).
[21] E. C. C. Yeh and K. N. Tu, J. Appl. Phys. **88**, 5680 (2000).
[22] K. L. Grosse, M. Bae, F. Lian, E. Pop, and W. P. King, Nature Nanotech. **6**, 287 (2011).
[23] T. W. L. Sanford, J. A. Halbleib, J. W. Poukey, A. L. Pregenzer, R. C. Pate, C. E. Heath, R. Mock, G. A. Mastin, D. C. Ghiglia, T. J. Roemer, P. W. Spence, and G. A. Proulx, J. Appl. Phys. **66**, 10 (1989).
[24] M. E. Cuneo, IEEE Transactions on Dielectrics and Electrical Insulation **6**, 469 (1999).
[25] B. T. Hutsel, P. A. Corcoran, M. E. Cuneo, M. R. Gomez, M. H. Hess, D. D. Hinshelwood, C. A. Jennings, G. R. Laity, D. C. Lamppa, R. D. McBride, J. K. Moore, A. Myers, D. V. Rose, S. A. Slutz, W. A. Stygar, E. M. Waisman, D. R. Welch, and B. A. Whitney, Phys. Rev. Accel. Beams **21**, 030401 (2018).
[26] N. Bennett, D. R. Welch, C. A. Jennings, E. Yu, M. H. Hess, B. T. Hutsel, G. R. Laity, J. K. Moore, D. V. Rose, K. Peterson, and M. E. Cuneo, Phys. Rev. Accel. Beams **22**, 120401 (2019).

[27] D. R. Welch, N. Bennett, T. C. Genoni, D. V. Rose, C. Thoma, C. Miller, and W. A. Stygar, Phys. Rev. Accel. Beams **22**, 070401 (2019).
[28] D. V. Rose, E. A. Madrid, D. R. Welch, R. E. Clark, C. B. Mostrom, W. A. Stygar, and M. E. Cuneo, Phys. Rev. Accel. Beams **18**, 030402 (2015).
[29] M. G. Haines, J. Plasma Physics **12**, 1 (1974).
[30] D. D. Ryutov, M. S. Derzon, and M. K. Matzen, Rev. Modern Physics **72**, 167 (2000).
[31] V. I. Oreshkin, Phys. Plasmas **15**, 092103 (2008).
[32] K. J. Peterson, D. B. Sinars, E. P. Yu, M. C. Herrmann, M. E. Cuneo, S. A. Slutz, I. C. Smith, B. W. Atherton, M. D. Knudson, and C. Nakhleh, Phys. Plasmas **19**, 092701 (2012).
[33] J. D. Pecover and J. P. Chittenden, Phys. Plasmas **22**, 102701 (2015).
[34] R. B. Baksht, A. G. Rousskikh, A. S. Zhigalin, V. I. Oreshkin, and A. P. Artyomov, Phys. Plasmas **22**, 103521 (2015).
[35] T. M. Hutchinson, T. J. Awe, B. S. Bauer, K. C. Yates, E. P. Yu, W. G. Yelton, and S. Fuelling, Phys. Rev. E **97**, 053208 (2018).
[36] A. M. Steiner, P. C. Campbell, D. A. Yager-Elorriaga, N. M. Jordan, R. D. McBride, Y. Y. Lau, and R. M. Gilgenbach, IEEE Trans. Plasma Sci. **46**, 3753 (2018).
[37] S. F. Garanin, and S. D. Kuznetsov, J. Appl. Phys. **123**, 133301 (2018).
[38] E. G. Harris, Phys. Fluids **5**, 1057 (1962).
[39] Y. Zhou, Phys. Rep. **723-725**, 1 (2017).
[40] D. E. Ruiz, Phys. Plasmas **27**, 022121 (2020).
[41] K. C. Yates, manuscript submitted to Phys. Plasmas.
[42] A. B. Sefkow, Bull. Am. Phys. Soc. **61** (2016).
[43] H. Lamb, *Hydrodynamics, Sixth Edition* (Dover, New York, 1932), 65.
[44] P. Zhang, Y. Y. Lau, and R. M. Gilgenbach, J. Appl. Phys. **105**, 114908 (2009).
[45] C. Pérez-Arancibia, P. Zhang, O. P. Bruno, and Y. Y. Lau, J. Appl. Phys. **116**, 124904 (2014).
[46] L. M. Milne-Thomson, *Theoretical Hydrodynamics, Fifth Edition* (Dover, New York, 1968).
[47] L. D. Landau and E. M. Lifshitz, *Fluid Mechanics, 2nd edition* (Butterworth-Heinemann, Oxford, 1987).
[48] D. D. Ryutov, Phys. Plasmas **25**, 100501 (2018).
[49] D. Bolster, R. E. Hershberger, and R. J. Donnelly, Phys. Today **64**, 42 (2011).
[50] L. Levitov and G. Falkovich, Nature Phys. **12**, 672 (2016).
[51] J. A. Sulpizio, L. Ella, A. Rozen, J. Birkbeck, D. J. Perello, D. Dutta, M. Ben-Shalom, T. Taniguchi, K. Watanabe, T. Holder, R. Queiroz, A. Principi, A. Stern, T. Scaffidi, A. K. Geim, and S. Ilani, Nature **576**, 75 (2019).
[52] D. A. Bandurin, I. Torre, R. K. Kumar, M. B. Shalom, A. Tomadin, A. Principi, G. H. Auton, E. Khestanova, K. S. Novoselov, I. V. Grigorieva, L. A. Ponomarenko, A. K. Geim, and M. Polini, Science **351**, 1055 (2016).
[53] M. Mendoza, H. J. Herrmann, and S. Succi, Phys. Rev. Lett. **106**, 156601 (2011).
[54] H. A. Haus and J. R. Melcher, *Electromagnetic Fields and Energy* (Prentice-Hall, Englewood Cliffs, New Jersey, 1989).
[55] R. D. McBride, S. A. Slutz, C. A. Jennings, D. B. Sinars, M. E. Cuneo, M. C. Herrmann, R. W. Lemke, M. R. Martin, R. A. Vesey, K. J. Peterson, A. B. Sefkow, C. Nakhleh, B. E. Blue, K. Killebrew, D. Schroen, T. J. Rogers, A. Laspe, M. R. Lopez, I. C. Smith, B. W. Atherton, M. Savage, W. A. Stygar, and J. L. Porter, Phys. Rev. Lett. **109**, 135004 (2012).
[56] R. L. Panton, *Incompressible Flow, Third Edition* (Wiley, New York, 2005).
[57] S. A. Chaikovsky, V. I. Oreshkin, I. M. Datsko, N. A. Labetskaya, and N. A. Ratakhin, Phys. Plasmas **21**, 042706 (2014).
[58] G. Schmidt, *Physics of High Temperature Plasmas, Second Edition* (Academic Press, New York, 1979), 129.
[59] D. B. Sinars, S. A. Slutz, M. C. Herrmann, R. D. McBride, M. E. Cuneo, C. A. Jennings, J. P. Chittenden, A. L. Velikovich, K. J. Peterson, R. A. Vesey, C. Nakhleh, E. M. Waisman, B. E. Blue, K. Killebrew, D. Schroen, K. Tomlinson, A. D. Edens, M. R. Lopez, I. C. Smith, J. Shores, V. Bigman, G. R. Bennett, B. W. Atherton, M. Savage, W. A. Stygar, G. T. Leifeste, and J. L. Porter, Phys. Plasmas **18**, 056301 (2011).
[60] H. Knoepfel, *Pulsed High Magnetic Fields* (North-Holland Publishing Company, Amsterdam, 1970).
[61] D. J. Griffiths, *Introduction to Electrodynamics, Second Edition* (Prentice Hall, Englewood Cliffs, New Jersey, 1989), 369.
[62] S. M. Ponomarev, U.S.S.R. Comput. Maths. Math. Phys. **28**, 177 (1988).
[63] O. Schnitzer, Phys. Plasmas **21**, 082306 (2014).
[64] A. C. Robinson and C. J. Garasi, Computer Physics Communications **164**, 408 (2004).
[65] T. Sjostrom, S. Crockett, and S. Rudin, Phys. Rev. B **94**, 144101 (2016).
[66] M. P. Desjarlais, J. D. Kress, and L. A. Collins, Phys. Rev. E **66**, 025401(R) (2002).

Physics of Plasmas

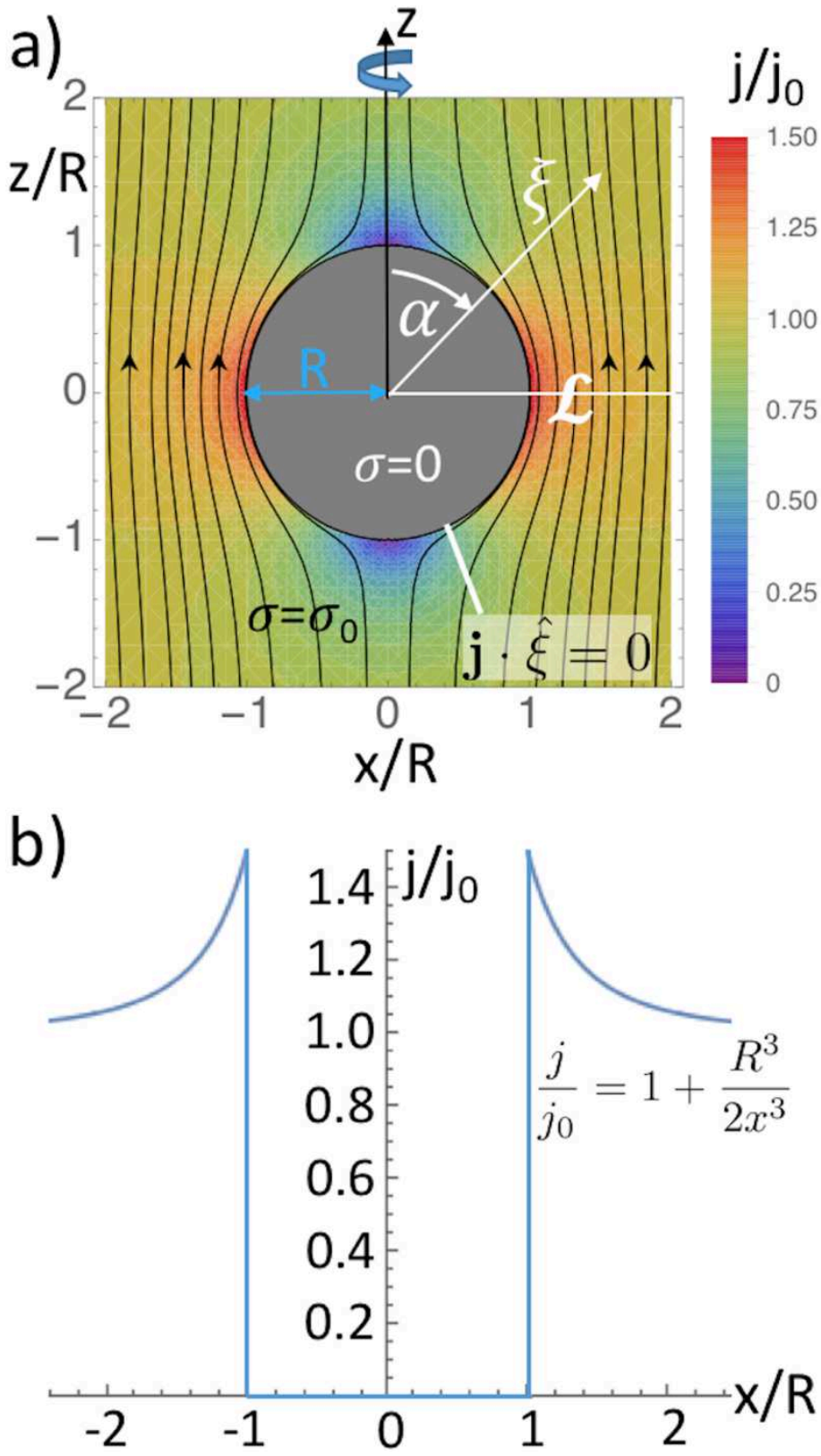

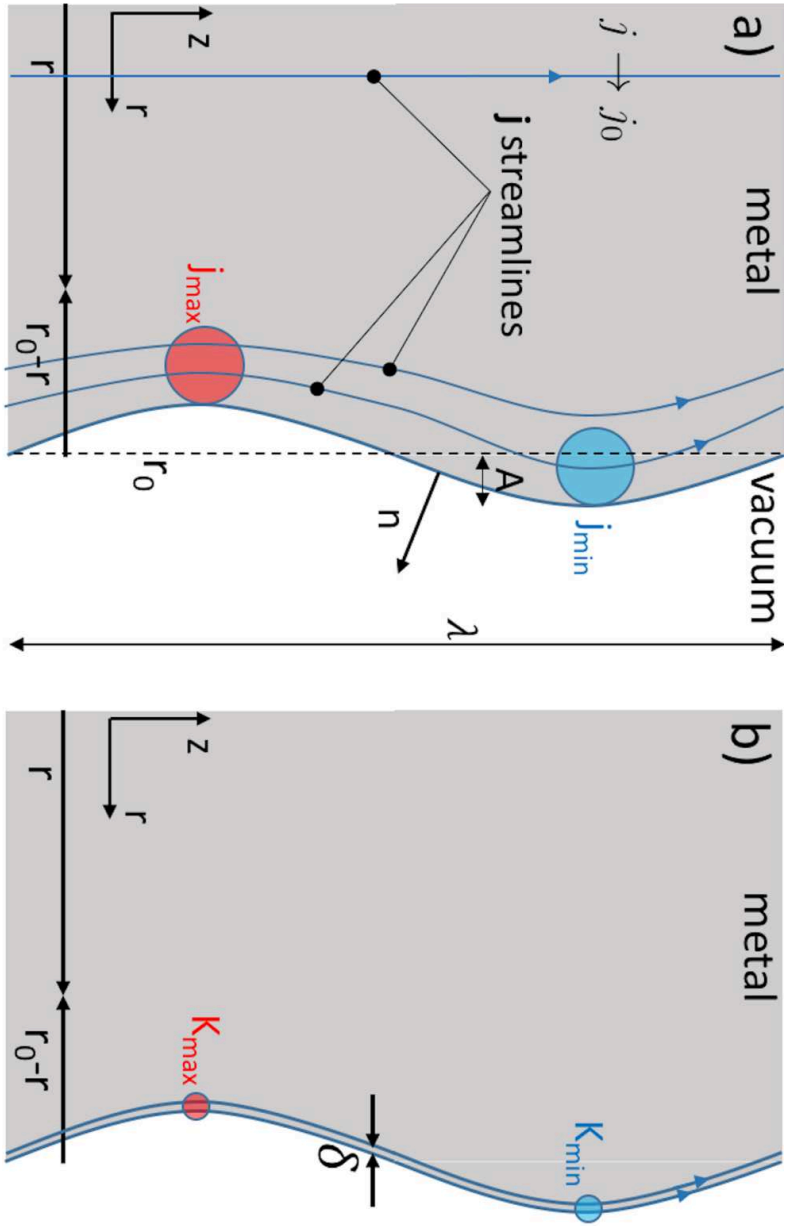

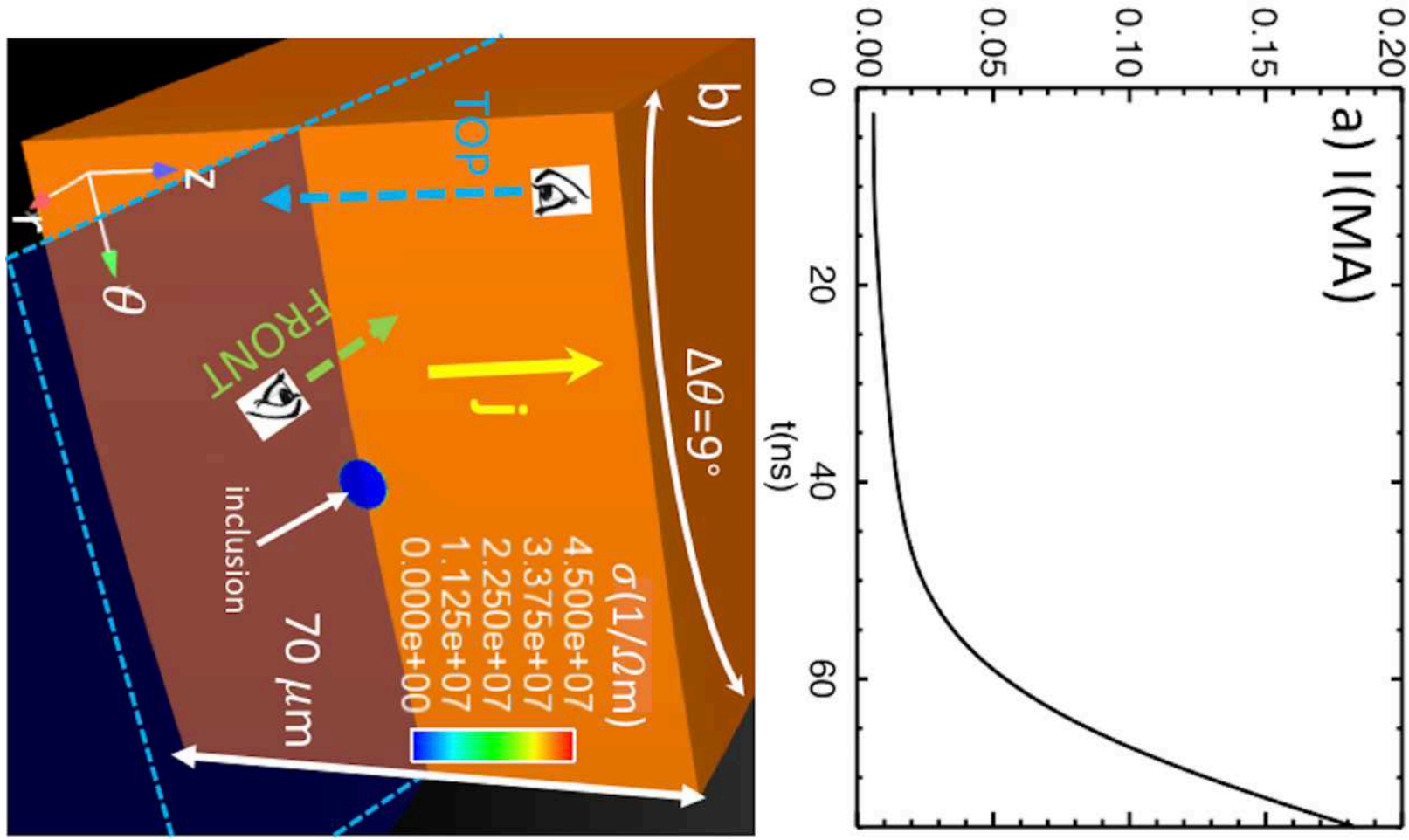

Physics of Plasmas

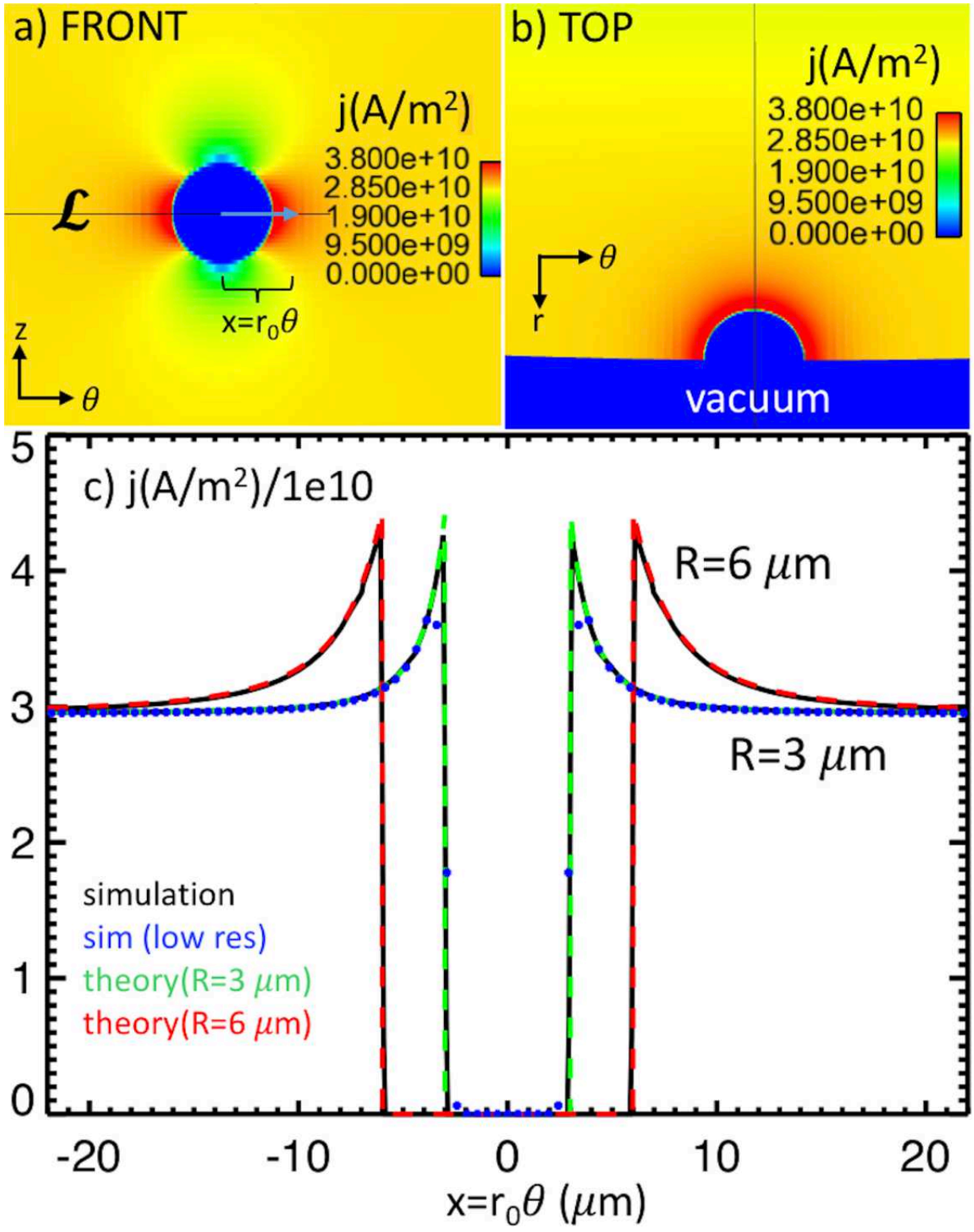

Physics of Plasmas

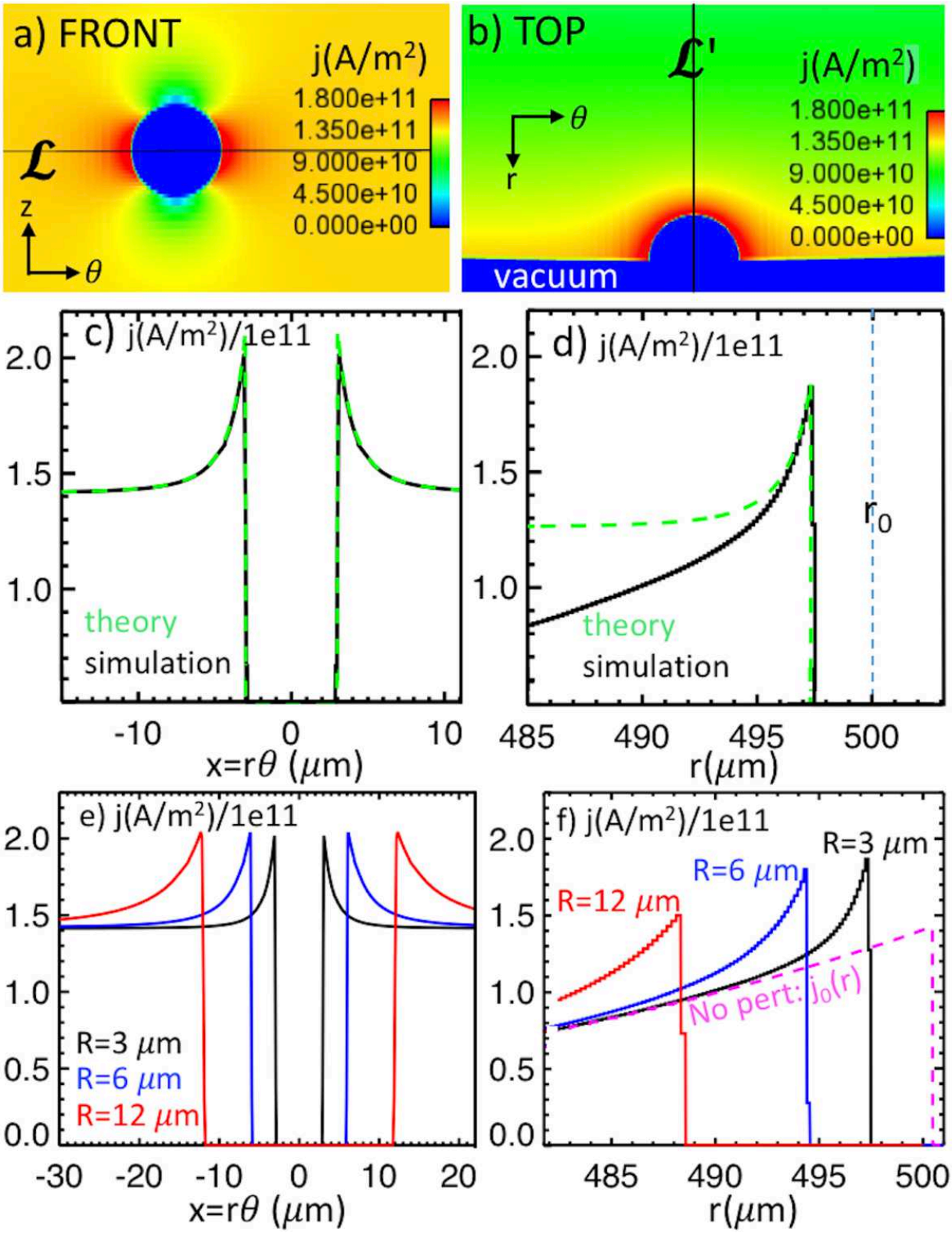

Physics of Plasmas

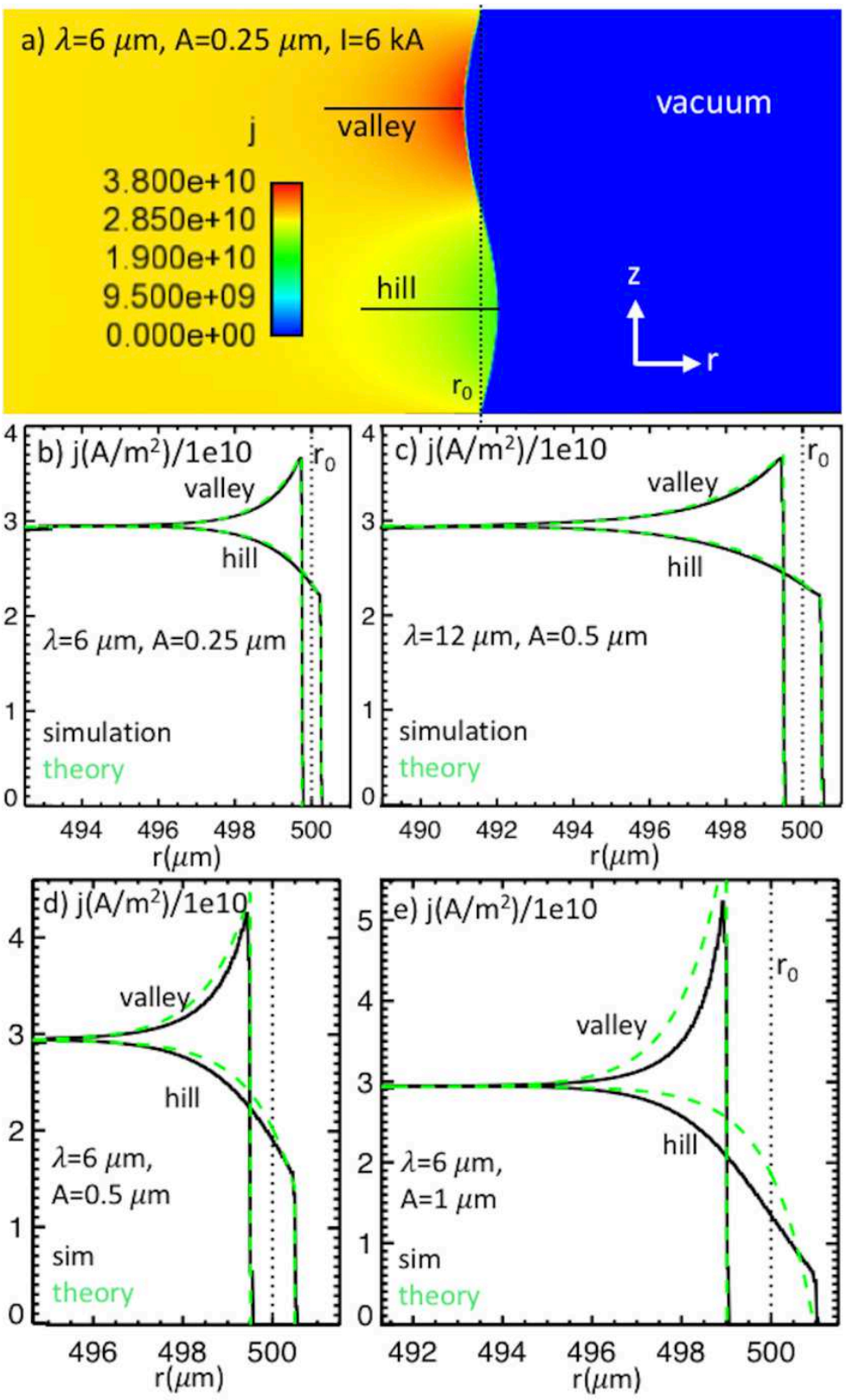

Physics of Plasmas